Journal of Physics D: Applied Physics

PAPER

Particle trapping, size-filtering, and focusing in the nonthermal plasma synthesis of sub-10 nanometer particles

To cite this article: Zichang Xiong *et al* 2022 *J. Phys. D: Appl. Phys.* **55** 235202

IOP Publishing Journal of Physics D: Applied Physics
J. Phys. D: Appl. Phys. **55** (2022) 235202 (13pp) https://doi.org/10.1088/1361-6463/ac57de

Particle trapping, size-filtering, and focusing in the nonthermal plasma synthesis of sub-10 nanometer particles

Zichang Xiong[1,7], Steven Lanham[2,7], Eric Husmann[3,7], Gunnar Nelson[4], Mohammad Ali Eslamisaray[1], Jordyn Polito[2], Yaling Liu[1], John Goree[5], Elijah Thimsen[3,*], Mark J Kushner[6,*] and Uwe R Kortshagen[1,*]

[1] Department of Mechanical Engineering, University of Minnesota, 111 Church Street SE, Minneapolis, MN 55455, United States of America
[2] Department of Chemical Engineering, University of Michigan, 2300 Hayward St, Ann Arbor, MI 48109-2136, United States of America
[3] Department of Energy, Environmental and Chemical Engineering, Washington University in Saint Louis, Saint Louis, MO 63130, United States of America
[4] Department of Chemical Engineering and Materials Science, University of Minnesota, 421 Washington Ave SE, Minneapolis, MN 55455, United States of America
[5] Department of Physics and Astronomy, The University of Iowa, Iowa City, IA, 52242, United States of America
[6] Department of Electrical Engineering and Computer Science, University of Michigan, 1301 Beal Ave, Ann Arbor, MI 48109-2122, United States of America

E-mail: elijah.thimsen@wustl.edu, mjkush@umich.edu and kortshagen@umn.edu

Received 24 December 2021, revised 22 February 2022
Accepted for publication 23 February 2022
Published 10 March 2022

Abstract

Low-pressure nonthermal flowing plasmas are widely used for the gas-phase synthesis of nanoparticles and quantum dots of materials that are difficult or impractical to synthesize using other techniques. To date, the impact of temporary electrostatic particle trapping in these plasmas has not been recognized, a process that may be leveraged to control particle properties. Here, we present experimental and computational evidence that, during their growth in the plasma, sub-10 nm silicon particles become temporarily confined in an electrostatic trap in radio-frequency excited plasmas until they grow to a size at which the increasing drag force imparted by the flowing gas entrains the particles, carrying them out of the trap. We demonstrate that this trapping enables the size filtering of the synthesized particles, leading to highly monodisperse particle sizes, as well as the electrostatic focusing of the particles onto the reactor centerline. Understanding of the mechanisms and utilization of such particle trapping will enable the design of plasma processes with improved size control and the ability to grow heterostructured nanoparticles.

Supplementary material for this article is available online

Keywords: nonthermal plasma, nanoparticle synthesis, particle trapping, size filtering

(Some figures may appear in color only in the online journal)

---

[7] Authors have made equal contributions.
[*] Authors to whom any correspondence should be addressed.

1361-6463/22/235202+13$33.00 Printed in the UK

1. Introduction

The term dusty plasma refers to a weakly ionized gas containing solid particulates [1, 2]. Over the past two decades, nonthermal dusty plasmas in low pressure flowing systems have become critically important sources for the synthesis of nanoparticles and quantum dots [3–8]. In these plasmas, energetic plasma electrons decompose molecular gaseous precursors, producing radicals, which lead to the nucleation and growth of nanoparticles. Based on the extreme nonequilibrium in these plasmas, with the temperature of electrons (several eV) exceeding the temperature of the gas atoms and plasma ions (near ambient) by about two orders of magnitude, dusty plasmas offer the ability to synthesize crystalline nanoparticles even of high melting point, including covalently bonded materials. This capability is due to the selective heating of nanoparticles to temperatures far above the gas temperature [8] which enables the synthesis of nanocrystals that are commonly inaccessible to liquid phase synthesis [9–11]. Once the nanoparticles growing in the plasma reach a certain minimum size, they acquire a negative charge based on the higher mobility of free plasma electrons compared to that of plasma ions which suppresses agglomeration of larger nanoparticles as a result of the resulting Coulombic repulsion [12, 13]. This mechanism is widely credited with the ability of plasmas to produce nanoparticles with much more monodisperse size distributions than other gas-phase approaches [8].

Dust particles immersed in plasmas are subject to a variety of forces, including electrostatic, gas and ion drag, thermophoresis, Brownian motion, and gravity [14–22]. The relative magnitude of each force depends on the size of the particle and the plasma conditions. The plasmas of interest here are produced by application of radio frequency (RF) voltages, typically sustained in cylindrical reactors of up to a few cm in diameter and 10–15 cm length, operating at pressures of a few Torr with nominal power deposition of up to about 50 W. The electrostatic force originates from the negative charge acquired by dust grains and the electric fields in the plasma. These electric fields are either ambipolar in nature, self-generated to confine the highly mobile electrons in a way that the plasma bulk is charged slightly positively compared to the surrounding reactor walls, or due to applied voltages, which for the plasmas of interest produce moderate electric fields of only a few V cm^{-1} in the bulk plasma and hundreds of V cm^{-1} in the bounding sheaths. In dusty plasmas containing micron-sized particles, particles can carry many thousands of elementary charges and electrostatic forces produced by the RF sheaths at the plasma boundary can be strong enough to balance the gravitational and ion drag forces, leading to particle levitation and trapping close to the plasma boundary sheath [2, 23]. In semiconductor processing, this trapping of particles was recognized as a problem as early as the 1990s [24], as dust particles that form during plasma processing can accumulate in these electrostatic particle traps and then drop onto the wafer being processed after the plasma is turned off.

Plasma reactors used for nanoparticle synthesis are fundamentally different from reactors used in semiconductor processing and those typically used to study the fundamental properties of dusty plasmas which are parallel plate, capacitively coupled systems [3, 4, 25, 26]. As noted above and shown schematically in figure 1(a), the plasmas typically used for nanoparticle synthesis are based on tubular laminar flow reactors, in which a plasma is excited either by capacitive or inductive coupling of RF power. Gas flow rates are commonly large so that the gas residence time in the reactor is on the order of milliseconds in order to limit particle growth to the nanometer size range.

For nanometer-sized particles, gravity does not play a significant role. Trapping, if it were to occur, would be the result of the balance between the electrostatic force and opposing forces such as the drag of the flowing neutral gas, the ion drag, and the thermophoretic force [14, 27]. In this context, trapping refers to nanoparticles which are temporarily quasi-stationary within the reactor and which continue to grow by reactions with radicals while in the trap. Particles are, indeed, collected as they flow out of the reactor so any trapping would be temporary or dynamic. However, to date, the likelihood and leveraging of particle trapping in the synthesis of nanoparticles with diameters of less than tens of nm has not been either realized or acknowledged. This lack of acknowledgement has resulted mainly from two reasons:

- The high concentration of nanoparticles during particle nucleation: during the initial nanoparticle nucleation event, the concentration of nanoparticles of less than a few nm in diameter commonly can exceed that of positive ions and plasma electrons by more than an order of magnitude [13]. These conditions imply that the average charge of nanoparticles in a plasma is less than one elementary charge. While the nanoparticle charge fluctuates stochastically due to the random collection of electrons and ions [12], nanoparticles are neutral for a significant fraction of time while in the plasma. (Large particles with sizes exceeding many tens of nm will be permanently negatively charged.) With particles of a few nm being neutral for long periods of time, they would presumedly not be subject to electrostatic trapping while still being subject to neutral drag and thermophoretic forces.
- In many studies, it has been found that the average nanoparticle size correlates nearly linearly with the residence time of particles in the plasma (and inversely with the gas flow velocity) [28]. These observations have been interpreted to mean that particles, while growing, travel through the reactor with the gas flow akin to a plug flow reactor and that the particle position in the reactor varies with time in a linear fashion. These processes are schematically shown in figures 1(b) and (c).

There have been limited reports of nanoparticle trapping during plasma synthesis. Nanoparticle trapping was observed in a laminar flow reactor with small gas flow speeds through the tube geared towards synthesizing large nanocrystals of several tens of nanometers in diameter [29]. This observation, *a priori*, was not inconsistent with the above reasoning because such large nanoparticles carry several tens of elementary charges and, in spite of stochastic charge fluctuations, are

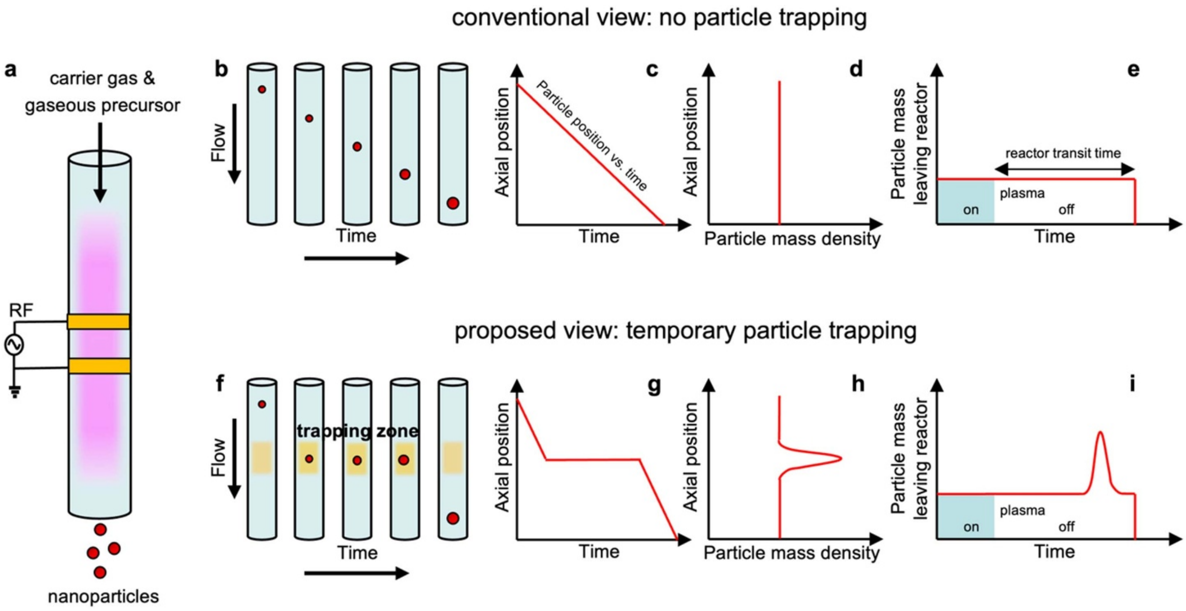

Figure 1. Overview of two scenarios of particle growth in nonthermal plasmas without and with particle trapping. (a) Schematic of laminar flow plasma reactor for nanoparticle synthesis. (b)–(e) Scenario without particle trapping and (f)–(i) with particle trapping. In the untrapped scenario (b)–(e) the particles flow through the reactor at a constant velocity as they continue to grow by reactions with radicals. Under the assumption of negligible radial losses to the reactor walls, the particle mass density, defined as the mass density of particles and unreacted precursor, is therefore constant along the reactor. When the plasma is extinguished, particle mass leaves the reactor at a constant rate until one transit time after the plasma turn-off. In the trapped scenario (f)–(i), the particles become temporarily trapped while continuing to grow, leading to a locally enhanced mass density in the trapping zone. When the plasma is turned off, removing the trap, this larger mass density is released and will appear as a peak in the rate of particle mass leaving the reactor.

likely negative all of the time. Furthermore, the gas drag that acts to remove particles from the electrostatic traps was small due to the low flow speeds. A recent simulation study was the first to point to the possibility of trapping even of particles even in the sub-10 nm regime [30]. While these simulations did not model the high particle concentrations that are present in actual synthesis reactors, they clearly indicated that even small particles that are electrically neutral for a fraction of their time in the plasma can experience trapping.

The present study provides the first experimental evidence, with computational verification, of the trapping of sub-10 nm particles during particle synthesis and introduces a new paradigm of utilizing trapping in nonthermal plasma synthesis for the size filtering of nanoparticles. The demonstration system is the growth of Si nanoparticles using Ar/SiH_4 gas mixtures in RF sustained plasmas at pressures of 1.1–6.5 Torr and powers of 5–20 W. Trapping was independently observed in multiple different reactor set-ups by two different research groups using different experimental techniques to analyze the presence of trapped particles. Experimental results were interpreted based on parametric Monte Carlo simulations and verified with full scale plasma reactor simulations.

2. Experimental approach and reactors

In situ detection of trapped sub-10 nm particles poses great difficulties. For larger particles, visible laser light scattering (LLS) is widely used [2, 23]. However, the scattered intensity for LLS rapidly becomes untenably small as the particle size is reduced. In particular, the Rayleigh scattering cross section scales with the sixth power of the particle diameter [31]. To overcome this unfavorable scaling, the only *in situ* detection method that we know of and that provides good sensitivity for particles smaller than 10 nm, is a destructive method—laser induced particle explosive evaporation (LIPEE) [32]. In this method, the diagnostic is not elastically scattered laser light, but rather the thermal glow from particles that are suddenly heated and evaporated by a pulsed laser. This LIPEE method has not been widely used in the dusty plasma literature since it was reported in 1994. This lack of use is perhaps due to the equipment that is required, which includes a powerful pulsed ultraviolet laser along with sensitive high-speed optical detection. For these reasons, our approach relies not on *in situ* detection of the particles, but instead on *ex situ* measurements.

Our experimental approach is based on the scheme detailed in figure 1 utilizing a time-resolved measurement of the particle mass at the exit of the reactor. For simplicity, we neglect in this figure the influence of radial losses of particles and chemical precursors, which occurs in an actual reactor, but will not significantly affect the argument that we present. If particle trapping during synthesis does not occur, the currently predominant view, particles move through the reactor with time in a linear fashion following the gas flow (figures 1(b) and (c)) while growing by reactions with the locally available precursor radicals. When radial losses are neglected, the particle mass density, defined by the mass density of the forming nanoparticles and that of the unreacted precursor, is constant along the reactor (figure 1(d)). Towards the exit of the reactor, the majority of the mass that has been transformed into particles

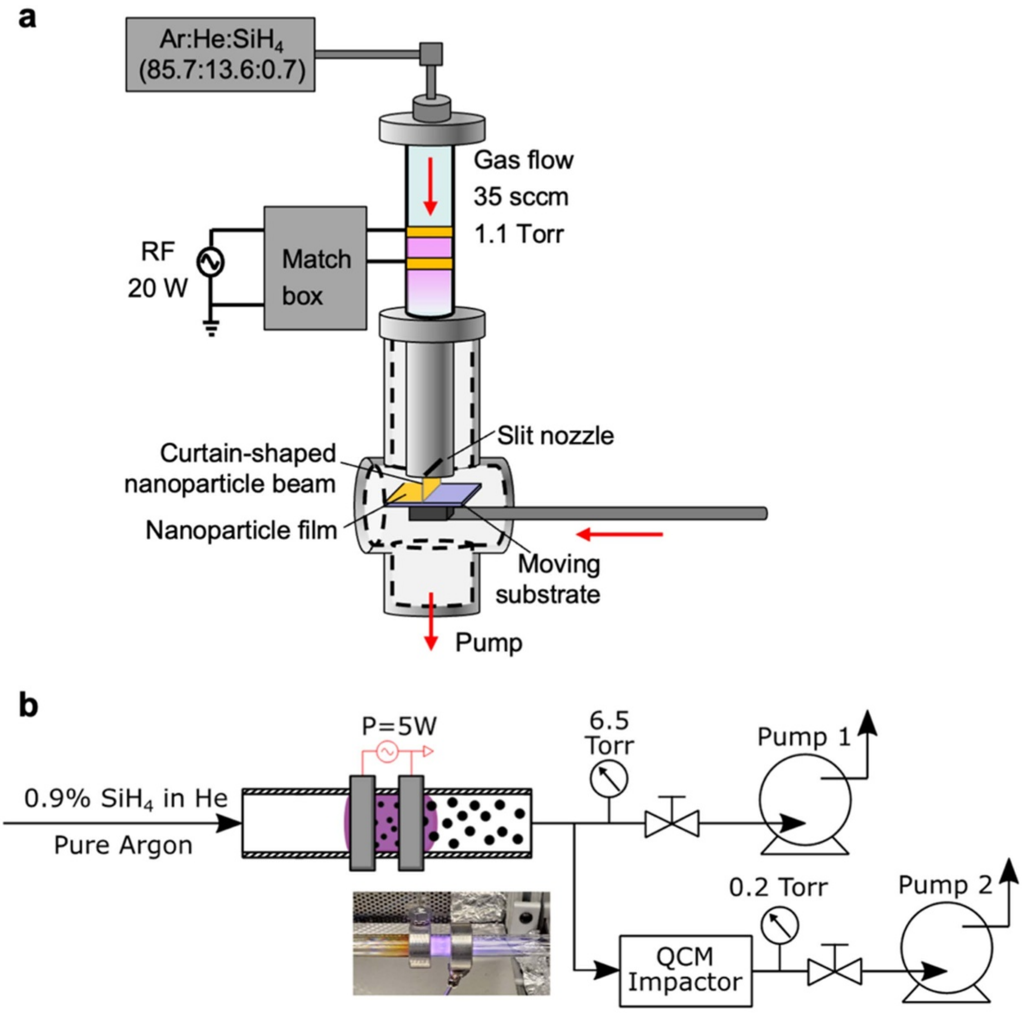

Figure 2. Schematics of two of the three plasma reactors used to investigate particle trapping. (a) Schematic of the UMN1 plasma synthesis reactor used to deposit silicon nanocrystals on a moving substrate. The deposited particle mass is analyzed by studying the optical absorbance of the particles on the substrate. (b) Schematic of the WUSTL plasma synthesis reactor. In this reactor, particle mass leaving the reactor is directly measured using a QCM.

can be collected and their mass measured. If the plasma is turned off, particle formation ceases and the collection of particles ceases after one gas transit time through the reactor following the moment of plasma turn-off (figure 1(e)).

Particle trapping significantly changes this picture. If nanoparticles are temporarily trapped, their motion through the plasma reactor is no longer linear in time (figures 1(f) and (g)). Particles are temporarily confined in a trapping zone but continue to grow due to the presence of the radical precursors. The electrostatic trapping force is roughly proportional to the particle diameter. However, in the Knudsen number range of relevance to low pressure plasmas, the gas drag force is proportional to the square of the particle diameter [33]. As a result, particles will be forced from the trap once they reach a critical size when drag by the gas flow dominates. However, since particles are temporarily stopped in their motion through the reactor, the particle mass density within the trapping zone exceeds that of the particles outside the trapping region (figure 1(h)). If the plasma is turned off and the particle mass at the reactor exit is measured, the trapped particles will appear as a peak in the particle mass leaving the reactor after the plasma is turned off (figure 1(i)).

To evaluate these two scenarios, three different plasma reactors were designed using different experimental methodologies to measure the particle mass leaving the reactor over time. The reactors are shown schematically in figure 2. The first reactor was resident at the University of Minnesota (UMN1). The plasma was generated by applying capacitively coupled RF power (frequency 13.56 MHz) to the quartz tubular reactor with 2.5 cm external diameter (2.2 cm internal diameter) and 20 cm length. The power was applied with a pair of ring electrodes 1 cm wide and separated by 2 cm at their centers. The operating conditions for the base case are an RF power of 20 W, flow rate of Ar/He/SiH_4 = 30/4.75/0.25 sccm and gas pressure of 1.1 Torr.

The nanoparticle cloud resulting from plasma synthesis was sent through a slit-shaped nozzle (0.5 mm × 12 mm) at the reactor exit and focused into a curtain-shaped beam of nanoparticles. These particles were deposited on a glass or silicon substrate that was translated through the nanoparticle beam at a constant velocity by a linear direct current (DC) servomotor.

The deposited particle mass was evaluated by measuring optical absorption of the particles deposited on a transparent glass substrate moving at a constant speed of 5 mm s^{-1}. The plasma was turned off during the substrate translation to collect both particles leaving the reactor in steady state operation and trapped particles. The substrate with deposited silicon nanoparticles was then placed on one exit port of a Labsphere 10 cm integrating sphere, illuminated with a light emitting diode (LED) emitting at 390 nm, and imaged using a digital camera (NIKON D7100). Raw files were converted to 16-bit TIFF format and the transmitted light intensity was measured as line intensity plots in ImageJ, using a bare glass substrate as a baseline. Absorbance was obtained as $A = -\log(I_t/I_0)$, where I_t is the transmitted light intensity and I_0 is the incident light intensity.

The delay time of the arrival of the trapped particles at the substrate after turning off the plasma was measured by a 240 frames-per-second camera (iPhone 12, Slo-mo mode). Accuracy of the arrival time was estimated as ±1 frame (1/240 s). The axial trapping position was determined by multiplying the arrival time by the gas flow velocity, which was determined by fitting particle arrival times versus the different axial positions of the electrode pair.

A second reactor similar in design to UMN1, also resident at the University of Minnesota was used to evaluate the consequences of particle growth on precursor density and deposition on the walls of the reactor. This reactor, UMN2, was a quartz tubular reactor having two diameters. The power was applied to the narrower portion of the tube, 0.7 cm internal diameter. The tube expanded downstream to 2.2 cm internal diameter. The plasma conditions were a gas pressure of 0.8–0.9 Torr and gas mixture of Ar/He/SiH_4 that was varied from 30/6.65/0.35 sccm to 30/13.3/0.7 sccm. RF power of 50 W was applied to a pair of 1 cm wide electrodes, separated by 2 cm center-to-center, that was located 2 cm upstream of the tube expansion.

The third reactor was resident at Washington University in St Louis (WUSTL). Similar to the UMN1 reactor, the plasma was generated by applying capacitively coupled RF power (frequency 13.56 MHz) to the quartz tubular reactor with 3.2 cm internal diameter. The power was applied with a pair of aluminum ring electrodes 1.4 cm wide and separated by 2.65 cm at their centers. The operating conditions for the base case are an RF power of 5 W, flow rate of Ar/He/SiH_4 = 51/0.991/0.009 sccm and gas pressure of 6.5 Torr. Following the reactor, 2.7% of the total flow was diverted to a quartz crystal microbalance (QCM) impactor. A 150 μm orifice was used to impact synthesized particles onto the quartz crystal. The mass loading on the quartz crystal was determined using the Sauerbrey equation [34]:

$$\Delta m = -\Delta f\left(\frac{A\sqrt{\rho_q \mu_q}}{2f_o^2}\right), \qquad (1)$$

where Δm is the change in the mass loading of the quartz crystal, Δf is the change in the quartz crystal resonance frequency, A is the effective crystal area (6.5 mm), ρ_q is the density of the quartz crystal (2.65 g cm^{-3}), μ_q is the shear modulus of the quartz crystal (2.95 × 10^{11} g cm^{-1} s^{-2}), and f_o is the resonant frequency of the fundamental mode of the quartz crystal (6 MHz).

Transmission electron microscope (TEM) imaging of the collected particles was performed using an FEI Talos F200x operating at an accelerating voltage of 200 kV as well as an FEI Tecnai T12 operating at 120 kV. To determine particle size distributions, nanoparticles were deposited directly onto thin holey carbon coated Cu TEM grids translated under the curtain-shaped particle beam in reactor UMN1. The diameters of 300 particles were then measured with ImageJ and their size distribution fit to a log-normal size distribution.

3. Observations of nanoparticle trapping

Silicon nanoparticles deposited on a silicon substrate translated with constant velocity under the exit nozzle of the UMN1 reactor are shown in figure 3(a). Initially, the particle deposition is essentially uniform (except for some nonuniformities caused by the not entirely constant speed of the motor drive). After turning off the plasma and emptying of the electrostatic trap, the deposition of a significantly larger amount of particles was observed corresponding to the arrival of trapped particles, consistent with the scenario described in figures 1(f)–(i). After the arrival of the trapped particles, the deposition of additional particles was observed corresponding to particles that were upstream of the trapping zone when the plasma was turned off. The curvature of the deposition in vertical direction is assumed to be caused by the laminar flow in the reactor with there being little slip at the surface of the tube. These conditions result in the gas close to the reactor wall to have a lower flow speed than at the center of the tube. The amount of mass corresponding to the trapped particles is about five times that of the particles leaving the reactor in steady state, shown in figure 3(b). The experiment was repeated for three different axial positions of the electrodes that would in turn determine the location of the electrostatic trap. From the delay of the arrival of the trapped particles with respect to the moment of plasma turn-off, the gas flow velocity was determined which then enabled the computation of the axial position of the trapped particles. As shown in figure 3(c), the trapping zone is located about 1.6 cm below the powered top electrode.

Results from the WUSTL plasma reactor, which was operated at significantly higher pressure than the UMN1 reactor, are shown in figures 3(d) and (e). In this reactor, the arrival of particles after leaving the reactor was significantly delayed due to the low flow rate in the gas lines leading to the QCM. A significant increase in the deposited mass after plasma turn-off, indicative of the arrival of trapped particles, is shown in figure 3(c). The mass deposition rate after the plasma was turned off was almost two orders of magnitude larger than the deposition rate during the steady-state plasma on phase,

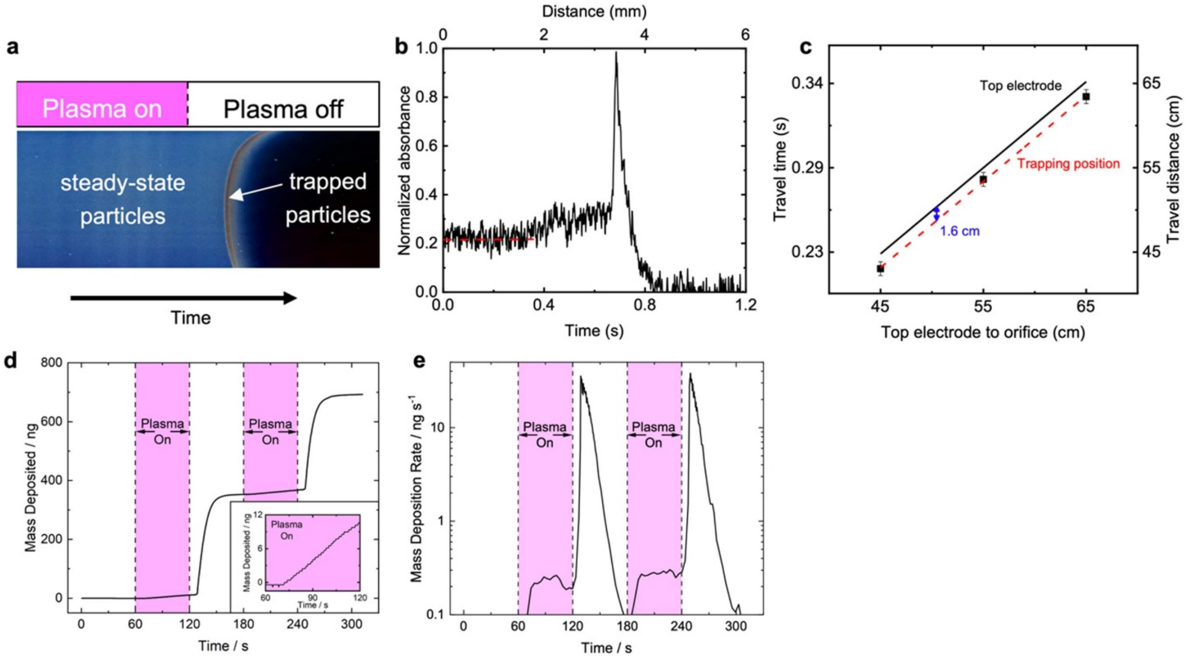

Figure 3. Experimental results demonstrating particle trapping in the synthesis of sub-10 nm silicon particles. (a)–(c) Results from the UMN1 reactor. (a) Photograph of particles deposited on a silicon substrate (to enable better photographic imaging) moving at constant speed below the reactor exit showing the deposition peak associated with trapped particles. (b) Absorbance of 390 nm light by silicon nanoparticles on the translated glass substrate. (c) Position of trapped particles derived from arrival time of particles after plasma turn-off for three different electrode positions. (d), (e) Results from WUSTL plasma reactor. (d) Particle mass deposited on a QCM over time and (e) particle mass deposition rate.

as shown in figure 3(e). This result suggests that the particle mass density in the particle trap is about a factor of 100 times larger than that outside of the trap. These results demonstrate that plasma parameters such as pressure and flow rates can be used to control the amount of particle mass that is trapped compared to that leaving in steady state.

It is also instructive to consider the deposition of a silicon film on the reactor walls, which occurs in actual reactors as an unwanted loss process of radicals, but was neglected in our simplified argument illustrated in figure 1. The silicon film deposition in a third plasma reactor, similar in design to the UMN1 reactor, which is typically used for the synthesis of sub-5 nm silicon particles, is shown in figure 4. For the higher flow rates associated with silicon nanocrystal formation (Ar/He/SiH$_4$ = 50/13.7/0.7 sccm), the deposition of a silicon film on the reactor walls is limited to the region upstream of the electrodes. If the silane precursor flow rate is lowered to a level that particle nucleation does not occur (Ar/He/SiH$_4$ = 50/6.65/0.35 sccm), and no particles are collected, the silicon film deposition is observed both upstream and downstream of the RF electrodes. These observations are consistent with the hypothesis that nanoparticles are trapped close to the RF electrodes at the higher silane flow rate. The trapped particles likely act as a sink for the silane precursor that leads to an almost complete precursor consumption in the region upstream and up to the RF electrodes. In the case of the lower silane flow, no particles form and the strong precursor sink around the electrodes is removed, leading to silicon deposition also downstream of the electrodes.

4. Evidence of size filtering

The sole observation of particle trapping during nonthermal plasma synthesis may be viewed as an interesting outcome of the plasma dynamics. However, its importance is significantly deeper because particle trapping acts as an inherent size filter in the plasma synthesis as particles need to reach a certain critical size before they can escape the particle trap. This concept is demonstrated in figure 5(a) which shows a TEM image of particles that are leaving the reactor in steady state operation. These are the particles that were trapped and grew to a size so that the gas drag overcame the electrostatic trapping force and liberated the particles from the trap. More than 300 particles were counted and their size distribution fit with a log-normal distribution with a mean size of 7.4 nm and a geometric standard deviation of 1.17. This geometric standard deviation is typical for nonthermal plasma synthesis but significantly smaller than those achieved in other gas-phase syntheses where nanoparticles are neutral and not prevented from agglomerating [35, 36]. Particles shown in figure 5(b) were collected after the plasma turn-off and are representative of the trapped particle deposit shown in figure 3(a). These particles exhibit a significant population of smaller particles that is not present in the particles that are collected in steady state. Accordingly, the log-normal size distribution of trapped particles has a mean size of 6 nm and a geometric standard deviation of 1.39. To our knowledge, this is the first demonstration of trapping acting as a size filter during the nonthermal plasma synthesis of sub-10 nm particles. Understanding this aspect may open new routes to designing

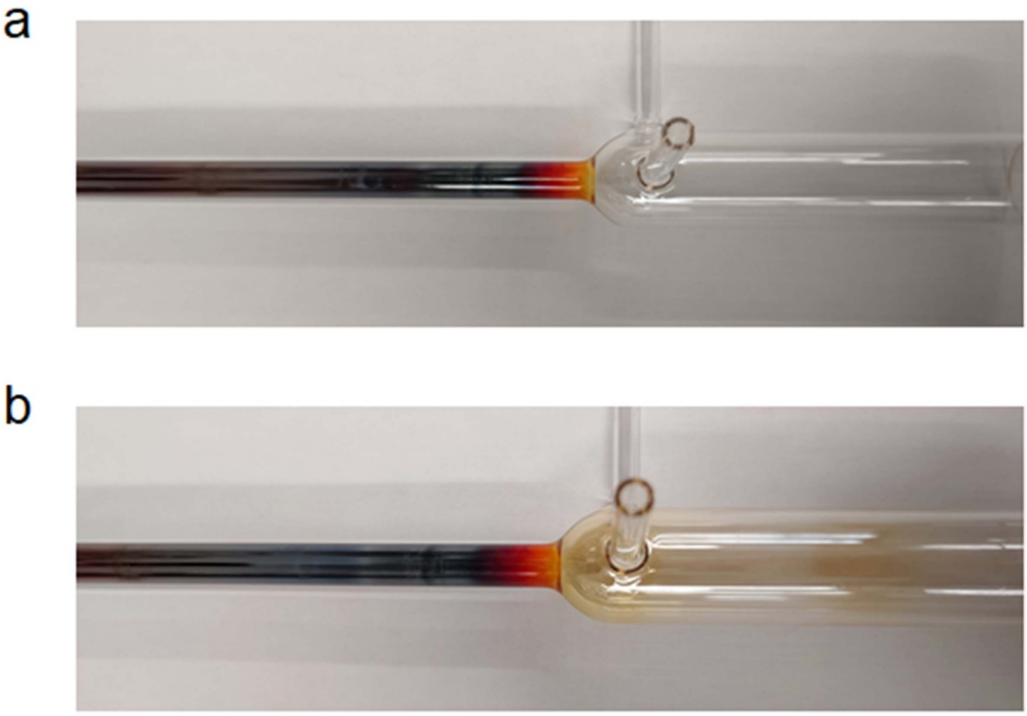

Figure 4. Images of the UMN2 reactor used for silicon quantum dot synthesis. The electrode pair was located 2 cm to the left of the tube expansion. (a) Photograph of a plasma reactor run with a silane flow rate ($Ar/He/SiH_4 = 50/13.3/0.7$ sccm) that leads to the formation and collection of $\sim$3 nm Si quantum dots. Note that deposition of a parasitic silicon film is only observed upstream (left) of the electrodes but not downstream (right) of the electrodes. This observation is consistent with the assumption that trapped particles around the electrode position act as sink of silicon precursor, preventing silicon film deposition downstream of the electrodes. (b) Photograph of the same plasma reactor operated at lower silane flow rate (0.35 sccm) so that particle nucleation and collection is avoided. Note that film deposition now also occurs downstream of the electrodes, suggesting that the precursor sink due to trapped particles is removed, because the precursor density is too low for particle nucleation.

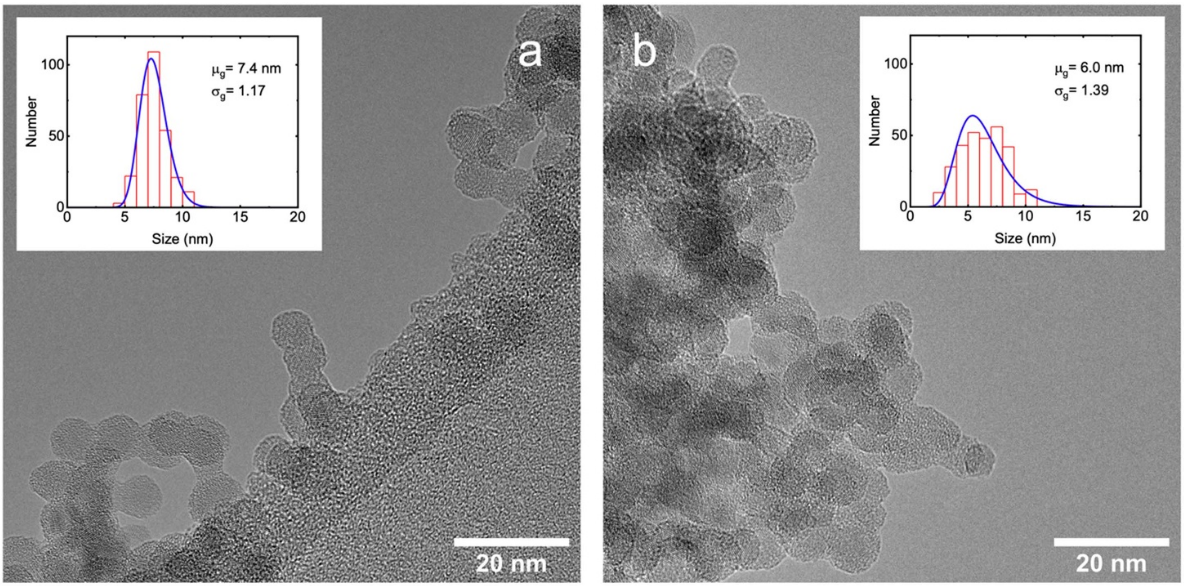

Figure 5. Particle trapping acting as a size filter in the nanoparticle synthesis with nonthermal plasmas. Transmission electron micrographs of silicon nanocrystals and associated size distributions (insets). (a) Particles that exit the plasma reactor in steady state and (b) particles that are representative of those collected from the trapping region after plasma turn-off.

plasma processes with even better size and composition control.

5. Parametric Monte Carlo simulation of particle trapping

Particle charge and particle trajectories were simulated with a one-dimensional Monte Carlo code implemented in MATLAB, shown schematically in the supplementary information figure S1 (available online at stacks.iop.org/JPhysD/55/235202/mmedia). In this simulation, pseudo-particles of a specified diameter are initiated at the entrance to the plasma reactor. Their size is kept constant during the simulation. The simulation is based on the assumption that the plasma is quasi-neutral. Due to the large concentration of nanoparticles in the physical system, the vast majority of electrons resides on the particles. However, in our simulation, a single nanoparticle is simulated at a time; hence, the effect of the electron attachment to nanoparticles is parametrically represented by an electronegativity n_i/n_e, with n_i the positive ion density and n_e the free electron density. In nanoparticle-forming argon-silane plasmas it has been observed that n_i often exceeds n_e by about two orders of magnitude, and that the density of negative ions is on the same order as n_e [37], because negative ions are consumed in particle nucleation. Hence, the charging of nanoparticles is described by the collection of electrons and positive ions, while negative ions are neglected.

The nanoparticle trajectories are integrated in time accounting for the gas drag force and electrostatic force until particles leave the reactor. Hence, an important input for this simulation is the time-averaged axial electric field profile, as the nanoparticles are too massive to follow the instantaneous RF electric field. An approximate electric field profile was derived by performing Comsol simulations for a pure argon plasma, as shown in the supplementary information figure S2. The time averaged electric field derived from these simulations, figure S2(d), was approximated by the simplified profiles in figure S2(e).

The simulation ran cyclically with a time step Δt of 100 ns. At every time step, a new position and charge for a particle was calculated. The initial particle had no charge and had a position of 10 cm from the outlet. Orbital motion limited theory [38] was then used to calculate collision frequencies of the particle with ions and electrons [39]:

$$\begin{aligned}\nu_{e,i} &= n_{e,i} S\left(\frac{k_{\mathrm{B}} T_{e,i}}{2\pi m_{e,i}}\right)^{1/2} \exp\left(-\frac{q_{e,i}\Phi_k}{k_{\mathrm{B}} T_{e,i}}\right), \qquad q_{e,i}\Phi_k \geq 0,\\ &= n_{e,i} S\left(\frac{k_{\mathrm{B}} T_{e,i}}{2\pi m_{e,i}}\right)^{1/2} \left(1-\frac{q_{e,i}\Phi_k}{k_{\mathrm{B}} T_{e,i}}\right), \qquad q_{e,i}\Phi_k < 0,\end{aligned} \tag{2}$$

where $S = 4\pi R_{\mathrm{p}}^2$ is the particle surface area, $n_{e,i}$, $m_{e,i}$ and $T_{e,i}$ are density, mass and temperature of electrons and ions, respectively. Here $q_{e,i}$ represents $\mp e$ (with e the elementary charge) for electrons and ions, respectively; k_{B} is the Boltzmann constant, and $\Phi_k = \mathrm{Z}_k/4\pi\varepsilon_0 R_{\mathrm{p}}$ is the surface potential of a particle with radius R_{p} which carries a charge $\mathrm{Z}_k = ke$ (with k an integer), with ε_0 the vacuum dielectric constant. The probabilities of a particle colliding with an electron or and ion are $P_{e,i} = \Delta t \nu_{e,i}$. A specific event (collision with an ion or an electron) was chosen according to random Monte Carlo sampling.

The electrostatic force acting on a particle is $\overrightarrow{F_{\mathrm{E}}} = \vec{E} Z_k$, where $\vec{E}$ is the electric field. The gas drag force in the free molecular regime is $\overrightarrow{F_{\mathrm{D}}} = \left(\overrightarrow{v_{\mathrm{g}}} - \overrightarrow{v_{\mathrm{p}}}\right) \frac{4}{3} \rho_{\mathrm{g}} \bar{c}_{\mathrm{gas}} 1.36\pi R_{\mathrm{p}}{}^2$ [40], where $\overrightarrow{v_{\mathrm{g}}}$, $\overrightarrow{v_{\mathrm{p}}}$ are velocities of the gas and the particle, respectively, ρ_{g} is the gas density and $\bar{c}_{\mathrm{gas}} = \sqrt{\frac{8k_{\mathrm{B}}T_{\mathrm{g}}}{\pi m_{\mathrm{g}}}}$ is the average speed of gas molecules, with T_{g} the gas temperature and m_{g} the mass of gas molecules.

The Störmer–Verlet method [41] was applied to determine the particle trajectory. Given an initial position $\vec{z}_1$ and velocity $\vec{v}_1$, the particle position is advanced by a timestep Δt to a new position $\vec{z}_2$ using:

$$\vec{z}_2 = \vec{z}_1 + \vec{v}_1 (\Delta t) + \frac{\left(\overrightarrow{F_{\mathrm{E}}} + \overrightarrow{F_{\mathrm{D}}}\right)_1}{2m_{\mathrm{p}}} (\Delta t)^2, \tag{3}$$

where m_{p} is the particle mass. Subsequent particle positions are found from:

$$\vec{z}_{n+1} = 2\vec{z}_n - \vec{z}_{n-1} + \frac{\left(\overrightarrow{F_{\mathrm{E}}} + \overrightarrow{F_{\mathrm{D}}}\right)_n}{m_{\mathrm{p}}} (\Delta t)^2. \tag{4}$$

The particle velocity at each time step is evaluated as:

$$\vec{v}_{n+1} = \frac{\vec{z}_{n+1} - \vec{z}_n}{\Delta t}. \tag{5}$$

A single Monte Carlo simulation was run for 5×10^6 timesteps.

Results of the model are shown in figure 6. With the exception of the results shown in figure 6(f), simulations were performed for a typical positive ion density n_i of 5×10^{11} cm^{-3} and a free electron density n_e of 5×10^9 cm^{-3} resulting in an electronegativity $n_i/n_e = 100$. This degree of electronegativity is consistent with previous work on dusty plasmas forming silicon particles [42, 43]. Plasma electrons can dissociatively attach to silane or directly attach to radicals to form negative $\mathrm{SiH}_x{}^-$ ions and attach to the nanoparticles, whose density can exceed the positive ion density. The fraction of time that nanoparticles of three different sizes are in a certain charge state is shown in figure 6(a). Particles with a diameter of 1 nm are neutral or positively charged 78% of the time, while larger 5 nm particles are neutral 31% of the time. As a result of the long times that particles are neutral, one might conclude that small nanoparticles may not be trapped in the plasma.

The typical charging times are compared with the gas transit time through trapping region in figure 6(b), defined by the pink shaded region in figure 6(c) with a length of about 1 cm. In this region, the electrostatic force opposes the gas drag force and increases up to a maximum at $z = 4$ cm. Particle charging is so fast that neutral particles are likely to become negatively charged again before they are convected out of the

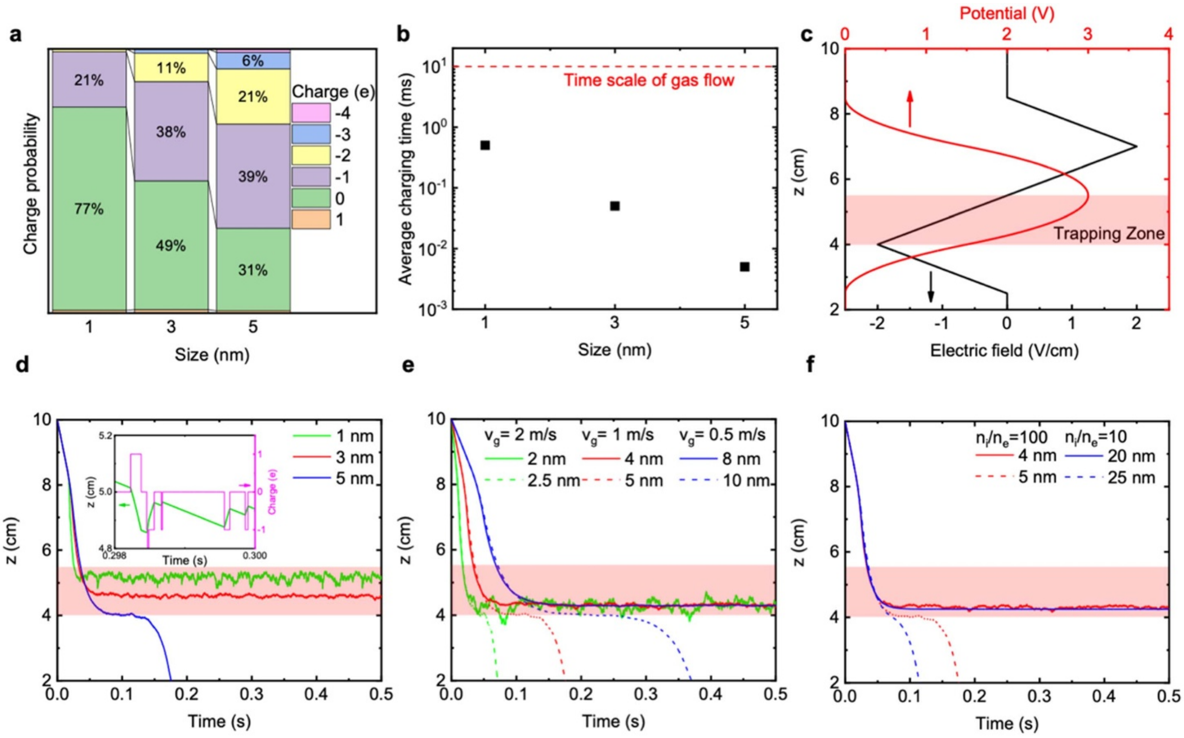

Figure 6. Parametric Monte Carlo model results of particle trapping. All results except (f) are for a positive ion density n_i of 5×10^{11} cm^{-3} and a free electron density n_e of 5×10^9 cm^{-3}. (a) Fraction of time that particles are found in a certain charge state for three different particle sizes. (b) Comparison of the typical charging times with the time scale of the gas flow through the trapping zone. (c) Electrostatic potential profile and electric fields. (d) Axial position of particles at three different diameters as function of time. The insert shows the particle trajectory and its correlation with the fluctuating particle charge for a 1 nm particle. (e) Influence of the gas flow velocity on the critical size for particle trapping. (f) Influence of plasma electronegativity on the critical size for particle trapping.

trapping zone. As a result, particles remain trapped, even if they are charged negatively only for a fraction of the time.

The trapping of particles in spite of their transient neutral states is demonstrated by the results in figure 6(d), which shows the axial locations of 1, 3 and 5 nm particles with time for a gas flow velocity of 100 cm s^{-1}. The smallest 1 nm particles enter the trapping zone and their position fluctuates in the axial direction as the particle charge changes. This is shown in the inset in figure 6(d), where particles follow the gas flow when they are neutral, but are drawn upstream again when they acquire a negative charge. For these conditions, 1 nm particles remain trapped indefinitely. Somewhat larger 3 nm sized particles behave similarly, but they assume a position deeper in the particle trap because they require a larger electrostatic force to balance the gas drag force. Particles with a 5 nm diameter are not confined in the trap. The particles are slowed down by the electrostatic force, but the force is insufficient to trap the particles. In an actual plasma reactor, the particle size does not remain constant, but particles grow due to the deposition of precursor. This means that the smallest particles are initially trapped at the top of the trap at the smallest electric fields. As particles grow, they sink deeper into the trap where the electric field increases. Finally, the electric field will be insufficient to balance the increasing gas drag and particles will be released from the trap.

The influence of gas flow velocity on the critical size for particle detrapping is shown by the results in figure 6(e). Since the gas drag force acting on trapped particles scales linearly with the gas flow speed, the critical size above which trapping does not occur varies inversely with the gas flow speed. The simulations reproduce the often observed linear dependence of particle size with the gas residence time in the reactor. However, the simulations suggest that the important time is not the residence time of the gas in the reactor but the extended time spent in the particle trap that allows particles to grow to larger sizes before leaving the trap.

The effect of plasma electronegativity on the critical size for detrapping is illustrated by the results in figure 6(f). As electronegativity in the plasma is reduced, the critical size for detrapping increases. This is due to the increased electron density at reduced plasma electronegativity, which produces more negatively charged particles and thus enhances electrostatic confinement. Both the impact of gas flow velocity and plasma electronegativity may be important parameters for designing trapping conditions in the plasma.

6. Full scale reactor simulations of particle growth and trapping

The nanoparticle and plasma dynamics leading to trapping and de-trapping of particles are functions of the spatially dependent electrostatic fields, gas flow, and particle growth rates. To investigate the influence of these processes, a two-dimensional

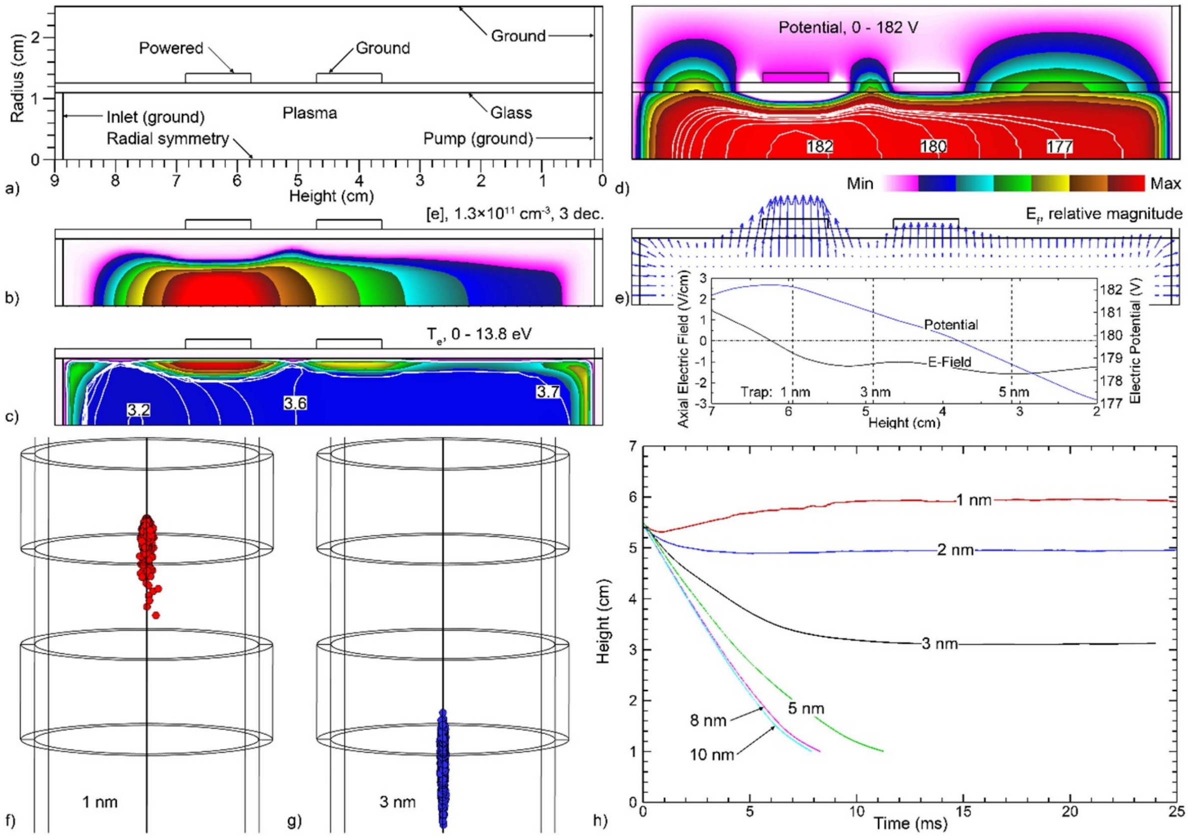

Figure 7. Reactor simulation and trapped particle locations. Self-consistent two-dimensional plasma hydrodynamics simulations for operating conditions of 1 Torr, gas flow rate 75 sccm, gas mixture Ar/He/SiH$_4$ = 99/0.9/0.1 with capacitively coupled power deposition of 10 W at a frequency of 10 MHz. Results are time averages over an RF period. (a) Model geometry, (b) electron density, (c) electron temperature, (d) plasma (electric) potential, and (e) electric field vectors with inset showing electric field and potential along the axis. Trapping locations are shown for (f) 1 nm particles and (g) 3 nm particles. (h) Average locations of particles as a function of time. The final locations are also indicated in the insert to (e).

plasma reactor model with an embedded three-dimensional nanoparticle trajectory and growth model were employed. The combination of the plasma reactor model, the hybrid plasma equipment model (HPEM), and the nanoparticle trajectory model, the dust transport simulator (DTS) are described in detail in [30]. The HPEM provides self-consistent electric fields, gas flow profiles, gas temperatures, charged particles fluxes, and radical fluxes. The DTS uses these values to predict the trajectories, statistical charging and trapping of growing nanoparticles while including all of the pertinent forces (electrostatic, fluid drag, ion drag, thermophoresis, gravity, Brownian motion, and particle-particle Coulomb force).

The HPEM/DTS was used to simulate the process conditions of a low pressure reactor similar to UMN1 described above, with the cylindrical model geometry shown in figure 7(a). The reactor length is 90 mm and diameter 20 mm with powered and grounded ring electrodes, and gas flowing left-to-right. The pressure was 1 Torr, the gas flow rate 75 sccm, the gas mixture Ar/He/SiH$_4$ = 99/0.9/0.1, and the capacitively coupled power deposition at a frequency of 10 MHz is 10 W. The electron density, electron temperature, electric potential, electric field vectors (with electric field and potential on axis) averaged over an RF cycle, are shown in figure 7. The electron density has a maximum value of 1.3×10^{11} cm^{-3} on axis at the position of the powered electrode. Due to the high conductivity of the plasma, the electron temperature is fairly constant in the bulk plasma, 3.2–3.7 eV, while extending above 10 eV in the sheath at the powered electrode. The amplitude of the applied RF voltage is 680 V with a self-generated DC bias on the tube wall of −217 V, which results in a maximum in the time averaged electric potential of 182 V. However, again due to the high conductivity of the plasma, the time averaged voltage drop across the bulk of the plasma is <10 V. This results in electric fields of hundreds of V cm^{-1} that are dominantly pointing outwards (confining for negative particles) at the boundaries of the plasma. The electric field along the axis at which particles are trapped is only a few V cm^{-1}.

Predictions of trapping locations for 1 and 3 nm particles are shown in figures 7(f)–(i). The 1 nm particles have trapping locations on axis that are nearly at the maximum of the plasma potential (see figure 7(e)). This focusing of the particles onto the axis results from radial electric fields which predominantly point outwards, thus accelerating particles radially inwards. The trapping locations are strewn along the axis for about 1 cm, a result of the charging and discharging of the particles.

When the particles discharge to be neutral, they drift downwards with the gas flow. When the particles recharge negatively, they drift back towards the maximum in the plasma potential. The 3 nm particles are also trapped on axis, though at a location further downstream beyond the maximum in the potential. The larger particles are more susceptible to the fluid drag forces and become trapped where the axial electric field provides a sufficient force to counter the fluid drag, approximately 1 V cm^{-1}, which occurs downstream of the trapping location of the 1 nm particles. The trapping sites are strewn along the axis for more than 1 cm.

The average locations for particle sizes of 1–10 nm as a function of time are shown in figure 7(h). A horizontal line (constant location) indicates that the particles are trapped. Particles falling below 1 cm are not trapped and exit the reactor. For the simulated conditions, de-trapping occurs for particle sizes of greater than about 4 nm when the neutral gas flow drag exceeds the ability of the plasma to electrostatically confine the particles. The trapping locations are at lower axial locations for larger particles where the confining axial electric fields are larger, as indicated in figure 7(e). The trends from the Monte Carlo simulations (figure 6) and those from the full two-dimensional simulations (figure 7) are in good agreement with each other, and with the experiments.

7. Concluding remarks

In this contribution, we showed through experiments performed on multiple plasma reactors as well as simulations with different levels of completeness that particle trapping through electrostatic forces does occur during the synthesis of sub-10 nm particles, a phenomenon that has generally not been recognized to date. We demonstrated that particles are trapped even if they are neutral for the majority of time that they spend in the trapping region due to a cycle of particles discharging and recharging. In actual plasma reactors, particles enter the trapping region and are spatially confined while growing through the continued accretion of precursor. Once particles reach a critical size such that the gas drag is sufficiently strong to overcome the electrostatic trapping force, particles are released from the trap. This critical size required for de-trapping narrows the collected particle size distribution since particles smaller than the critical size are confined and those that grow to larger than this critical size can escape and exit the reactor in steady state operation. Our numerical simulations suggest that the radial electric fields present in the particle trap lead to a focusing of the released particles onto the reactor centerline.

The observations reported here may establish a new paradigm for control of the nonthermal plasma synthesis of sub-10 nm particles. A better understanding of the trapping mechanism will enable a better control over particle sizes and more monodisperse size distributions than has been possible to date. The existence of trapping is of particular importance for the design of reactors for core–shell heterostructure nanoparticles [10, 44–46]. A better understanding of trapping will enable researchers to design plasma processes in which nanoparticles are either trapped or not trapped in the shell growth region. This will enable enhanced control over the range of core/shell diameter ranges than has been achieved at present. Moreover, the understanding of the particle focusing onto the centerline of the reactor is another important insight for the growth of heterostructure particles as it implies that all particles essentially experience the same growth conditions in the reactor, in spite of the parabolic flow velocity profile expected for laminar flow reactors.

However, the current study also leaves several open questions, such as whether particle trapping is a universal phenomenon or whether it is dependent on the nanoparticle material. For high gas flow rates most particles may not be trapped because the critical size for particles to be released from the trap by the gas drag decreases with increasing flow rates. There may also be electric field configurations in the plasma that do not support trapping. It is also not clear whether nanoparticles of insulators, semiconductors, or metals will be equally trapped as their charge states depend on their capacitance and secondary emission processes, and so depend on the materials work function or dielectric properties. These issues will need to be clarified to fully take advantage of particle trapping in nanoparticle synthesis as a design parameter. However, the current study demonstrates that gas flows and electric fields can be designed to utilize particle trapping to control particle sizes and size distributions.

Data availability statement

The data that support the findings of this study are available upon reasonable request from the authors.

Acknowledgments

This research was supported by the Army Research Office under MURI Grant W911NF-18-1-0240. These results were also based upon work supported by the US Department of Energy, Office of Science, Office of Fusion Energy Sciences under Award Number and DE-SC0020232. Parts of this work were carried out in the Characterization Facility, University of Minnesota, which receives partial support from the US National Science Foundation through the MRSEC (Award Number DMR-2011401) and the NNCI (Award Number ECCS-2025124) programs.

ORCID iDs

Zichang Xiong https://orcid.org/0000-0001-6486-1166
Steven Lanham https://orcid.org/0000-0001-9715-4134
Eric Husmann https://orcid.org/0000-0002-9968-8460
Elijah Thimsen https://orcid.org/0000-0002-7619-0926
Mark J Kushner https://orcid.org/0000-0001-7437-8573
Uwe R Kortshagen https://orcid.org/0000-0001-5944-3656

References

[1] Piel A 2017 *Plasma Physics: An Introduction to Laboratory, Space, and Fusion Plasmas* (Berlin: Springer)

[2] Melzer A 2019 *Physics of Dusty Plasmas* (Berlin: Springer)

[3] Knipping J, Wiggers H, Rellinghaus B, Roth P, Konjhodzic D and Meier C 2004 Synthesis of high purity silicon nanoparticles in a low pressure microwave reactor *J. Nanosci. Nanotechnol.* **4** 1039–44

[4] Mangolini L, Thimsen E and Kortshagen U 2005 High-yield plasma synthesis of luminescent silicon nanocrystals *Nano Lett.* **5** 655–9

[5] Chen T, Reich K V V, Kramer N J N J, Fu H, Kortshagen U R U R and Shklovskii B I I 2016 Metal–insulator transition in films of doped semiconductor nanocrystals *Nat. Mater.* **15** 299–303

[6] Meinardi F, Ehrenberg S, Dhamo L, Carulli F, Mauri M, Bruni F, Simonutti R, Kortshagen U and Brovelli S 2017 Highly efficient luminescent solar concentrators based on earth-abundant indirect-bandgap silicon quantum dots *Nat. Photon.* **11** 177–85

[7] Xia P, Raulerson E K, Coleman D, Gerke C S, Mangolini L, Tang M L and Roberts S T 2020 Achieving spin-triplet exciton transfer between silicon and molecular acceptors for photon upconversion *Nat. Chem.* **12** 137–44

[8] Kortshagen U R, Sankaran R M M, Pereira R N, Girshick S L, Wu J J and Aydil E S 2016 Nonthermal plasma synthesis of nanocrystals: fundamental principles, materials, and applications *Chem. Rev.* **116** 11061–127

[9] Alvarez Barragan A, Ilawe N V, Zhong L, Wong B M and Mangolini L 2017 A non-thermal plasma route to plasmonic TiN nanoparticles *J. Phys. Chem.* C **121** 2316–22

[10] Exarhos S, Alvarez-Barragan A, Aytan E, Balandin A A and Mangolini L 2018 Plasmonic core-shell zirconium nitride-silicon oxynitride nanoparticles *ACS Energy Lett.* **3** 2349–56

[11] Uner N B and Thimsen E 2020 Nonequilibrium plasma aerotaxy of size controlled GaN nanocrystals *J. Phys. D: Appl. Phys.* **53** 095201

[12] Matsoukas T, Russell M and Smith M 1996 Stochastic charge fluctuations in dusty plasmas *J. Vac. Sci. Technol.* A **14** 624–30

[13] Schweigert V A and Schweigert I V 1996 Coagulation in a low-temperature plasma *J. Phys. D: Appl. Phys.* **29** 655–9

[14] Barnes M S, Keller J H, Forster J C, O'Neill J A and Coultas D K 1992 Transport of dust particles in glow-discharge plasmas *Phys. Rev. Lett.* **68** 313–6

[15] Fortov V E, Khrapak A G, Khrapak S A, Molotkov V I and Petrov O F 2004 Dusty plasmas *Phys.-Usp.* **47** 447–92

[16] Fortov V, Ivlev A, Khrapak S, Khrapak A and Morfill G 2005 Complex (dusty) plasmas: current status, open issues, perspectives *Phys. Rep.* **421** 1–103

[17] Khrapak S and Morfill G 2009 Basic processes in complex (dusty) plasmas: charging, interactions, and ion drag force *Contrib. Plasma Phys.* **49** 148–68

[18] Thomas H M, Schwabe M, Pustylnik M Y, Knapek C A, Molotkov V I, Lipaev A M, Petrov O F, Fortov V E and Khrapak S A 2019 Complex plasma research on the International Space Station *Plasma Phys. Control. Fusion* **61** 014004

[19] Staps T J A, van de Ketterij M I, Platier B and Beckers J 2021 The underexposed effect of elastic electron collisions in dusty plasmas *Commun. Phys.* **4** 231

[20] Gopalakrishnan R and Hogan C J 2012 Coulomb-influenced collisions in aerosols and dusty plasmas *Phys. Rev.* E **85** 026410

[21] Ono T, Kortshagen U R and Hogan C J 2020 Ion attachment rates and collection forces on dust particles in a plasma sheath with finite ion inertia and mobility *Phys. Rev.* E **102** 063212

[22] Ashrafi K S, Yousefi R, Chen M, Matthews L S and Hyde T W 2020 Dust as probes: determining confinement and interaction forces *Phys. Rev.* E **102** 1–10

[23] Praburam G and Goree J 1994 Observations of particle layers levitated in a radio-frequency sputtering plasma *J. Vac. Sci. Technol.* A **12** 3137–45

[24] Selwyn G S, Heidenreich J E and Haller H L 1990 Particle trapping phenomena in radio frequency plasmas *Appl. Phys. Lett.* **57** 1876

[25] Gorla C R, Liang S, Tompa G S, Mayo W E and Lu Y 1997 Silicon and germanium nanoparticle formation in an inductively coupled plasma reactor *J. Vac. Sci. Technol.* A **15** 860

[26] Sankaran R M, Holunga D, Flagan R C and Giapis K P 2005 Synthesis of blue luminescent Si nanoparticles using atmospheric-pressure microdischarges *Nano Lett.* **5** 537–41

[27] Le Picard R, Markosyan A H, Porter D H, Girshick S L and Kushner M J 2016 Synthesis of silicon nanoparticles in nonthermal capacitively-coupled flowing plasmas: processes and transport *Plasma Chem. Plasma Process.* **36** 941–72

[28] Gresback R, Holman Z and Kortshagen U 2007 Nonthermal plasma synthesis of size-controlled, monodisperse, freestanding germanium nanocrystals *Appl. Phys. Lett.* **91** 093119

[29] Bapat A, Anderson C, Perrey C R, Carter C B, Campbell S A and Kortshagen U 2004 Plasma synthesis of single-crystal silicon nanoparticles for novel electronic device applications *Plasma Phys. Control. Fusion* **46** B97–109

[30] Lanham S J, Polito J, Shi X, Elvati P, Violi A and Kushner M J 2021 Scaling of silicon nanoparticle growth in low temperature flowing plasmas *J. Appl. Phys.* **130** 163302

[31] Bohren C F and Huffman D R 2008 *Absorption and Scattering of Light by Small Particles* (New York: Wiley)

[32] Boufendi L, Hermann J, Bouchoule A, Dubreuil B, Stoffels E, Stoffels W W and de Giorgi M L 1994 Study of initial dust formation in an Ar-SiH$_4$ discharge by laser induced particle explosive evaporation *J. Appl. Phys.* **76** 148–53

[33] Friedlander S K 2000 *Smoke, Dust, and Haze—Fundamentals of Aerosol Dynamcis* (Oxford : Oxford University Press)

[34] Sauerbrey G 1959 Verwendung von Schwingquarzen zur Wägung dünner Schichten und zur Mikrowägung *Z. Phys.* **155** 206–22

[35] Lai F, Friedlander S, Pich J and Hidy G 1972 The self-preserving particle size distribution for Brownian coagulation in the free-molecule regime *J. Colloid Interface Sci.* **39** 395–405

[36] Landgrebe J D and Pratsinis S E 1990 A discrete-sectional model for particulate production by gas-phase chemical reaction and aerosol coagulation in the free-molecular regime *J. Colloid Interface Sci.* **139** 63–86

[37] Agarwal P and Girshick S L 2014 Numerical modeling of an RF argon-silane plasma with dust particle nucleation and growth *Plasma Chem. Plasma Process.* **34** 489–503

[38] Allen J E, Annaratone B M and de Angelis U 2000 On the orbital motion limited theory for a small body at floating potential in a Maxwellian plasma *J. Plasma Phys.* **63** 299–309

[39] Kortshagen U and Bhandarkar U 1999 Modeling of particulate coagulation in low pressure plasmas *Phys. Rev.* E **60** 887–98

[40] Epstein P S 1924 On the resistance experienced by spheres in their motion through gases *Phys. Rev.* **23** 710

[41] Verlet L 1967 Computer 'experiments' on classical fluids. I. Thermodynamical properties of Lennard-Jones molecules *Phys. Rev.* **159** 98–103

[42] Agarwal P and Girshick S L 2012 Sectional modeling of nanoparticle size and charge distributions in dusty plasmas *Plasma Sources Sci. Technol.* **21** 055023

[43] Mamunuru M, Le Picard R, Sakiyama Y and Girshick S L 2017 The existence of non-negatively charged dust particles in nonthermal plasmas *Plasma Chem. Plasma Process.* **37** 701–15

[44] Mehringer C, Kloner C, Butz B, Winter B, Spiecker E and Peukert W 2015 Germanium-silicon alloy and core–shell nanocrystals by gas phase synthesis *Nanoscale* **7** 5186–96

[45] Hunter K I, Held J T, Mkhoyan K A A and Kortshagen U R 2017 Nonthermal plasma synthesis of core/shell quantum dots: strained Ge/Si nanocrystals *ACS Appl. Mater. Interfaces* **9** 8263–70

[46] Yasar-Inceoglu O, Zhong L L and Mangolini L 2015 Core/shell silicon/polyaniline particles via in-flight plasma-induced polymerization *J. Phys. D: Appl. Phys.* **48** 314009